Journal of Nuclear Materials 396 (2010) 20–25

Contents lists available at ScienceDirect

Journal of Nuclear Materials

journal homepage: www.elsevier.com/locate/jnucmat

High heat flux testing of 12–14Cr ODS ferritic steels

G. Pintsuk [a], Z. Oksiuta [b,*], J. Linke [a], N. Baluc [b]

[a] Institute for Materials and Processes in Energy Systems, Forschungszentrum Julich GmbH, EURATOM Association, 52425 Julich, Germany
[b] Ecole Polytechnique Fédérale de Lausanne (EPFL), Centre de Recherches en Physique des Plasmas, Association Euratom-Confédération Suisse, 5232 Villigen, PSI, Switzerland

ARTICLE INFO

Article history:
Received 9 December 2008
Accepted 29 September 2009

ABSTRACT

The thermal performance of Fe–(12–14)Cr–2W–0.3Ti–0.3Y_2O_3 ODS reduced activation ferritic steels, which are considered as candidate first wall materials for the future fusion power reactors and were manufactured by mechanical alloying in hydrogen and hot isostatic pressing, was assessed by high heat flux (HHF) testing with the electron beam JUDITH facility at the Forschungszentrum Jülich (FZJ), Germany. An analysis of the microhardness and microstructure of the specimens was done before and after HHF tests.

In general, both materials present a ferritic (α-Fe, bcc) microstructure with a wide range of grain sizes from 100 to 500 nm up to a few micrometers. The coarse grains are almost dislocation-free, while the smaller ones are surrounded by tangles of dislocations. Oxide and carbide impurities (about a few hundreds nm in size) and a high density of Y–Ti–O nano-clusters, with a mean size of about 5 nm, are also present. The microhardness, density and tensile strength of the 14Cr material are slightly larger than those of the 12Cr material.

HHF tests revealed that there is no difference in thermal performance, level of degradation and erosion behaviour of 12Cr and 14Cr ODS steels. The onset of melting of the materials occurs for an energy density between 1 and 1.5 MJ/m^2. Below this value only some kind of thermal etching takes place. This is a significant improvement compared to stainless steel, for which severe plastic deformation at the material surface was observed.

1. Introduction

Oxide dispersion strengthened (ODS) reduced activation ferritic (RAF) steels appear as promising materials for application in fusion power reactors up to about 750 °C [1–3]. One of the major issues in the development of ODS RAF steels for first wall application is their thermal shock resistance. The electron beam high heat flux (HHF) JUDITH facility with an operating power of 60 kW is a well-adapted instrument for this kind of investigation and is, due to its location in a hot cell, also suitable for the testing of neutron-irradiated materials [4]. It is operating in a scanning mode with a scanning frequency in the GHz range in *x*- and *y*-directions and has a beam diameter at full width half maximum of ~1 mm. With regard to the fact that the energy absorption coefficient for electrons depends on the material and decreases with increasing Z-number, power densities in the GW/m^2 range can be applied on a correspondingly small area of typically 4×4 mm^2.

The plate supporting the tungsten tiles in the European dual-coolant lithium–lead (DCLL) breeding blanket concept and the cartridge within the finger-like parts of the European He-cooled diverter concept [5] are presently foreseen to be made of ODS EUROFER [6,7]. In fusion power reactors these plasma facing components will have to withstand very high heat fluxes up to about 10 MW/m^2 as well as transient heat load events. The use of ODS RAF steels with a higher creep strength up to about 750 °C and a reasonable fracture toughness at ambient and intermediate temperatures will provide these components with additional integrity margin and lifetime.

This work aimed at investigating and comparing the thermal shock response of two different Fe–(12–14)Cr–2W–0.3Ti–0.3Y_2O_3 ODS RAF steels, which were prepared by mechanically alloying elemental powders with yttria nano-particles in a hydrogen atmosphere followed by canning, degassing and Hot Isostatic Pressing (HIPping), by using the HHF JUDITH facility.

2. Experimental procedure

Two kinds of Fe–(12–14)Cr–2W–0.3Ti–0.3Y_2O_3 ODS RAF steels (in weight percent) were prepared by mechanically alloying elemental Fe, Cr, W, and Ti powders with 0.3 wt.% Y_2O_3 nano-particles in a hydrogen atmosphere and HIPping at 1150 °C for 4 h. Then, specimens with a size of Ø10 × 5 mm^3 were prepared for HHF tests. More detailed information about sample preparation is reported elsewhere [8,9]. The specimen surface was mechanically polished by SiC abrasive papers using a final grit of 1000. The microstructure of the specimens was studied using Optical Microscopy (OM) and Transmission Electron Microscopy (TEM). Samples

* Corresponding author.
E-mail address: oksiuta@pb.bialystok.pl (Z. Oksiuta).

0022-3115/$ - see front matter © 2009 Published by Elsevier B.V.
doi:10.1016/j.jnucmat.2009.09.022

for TEM were electrolytically thinned in a solution of methanol with 10% perchloric acid using a jet polishing "TenuPol 5" device (Struers). Microhardness measurements at the polished surface of the specimens were carried out by using a Vickers diamond pyramid and applying a load of 0.98 N for 15 s. Each result is the average of 15 measurements. HHF testing was conducted with the electron beam JUDITH facility at Forschungszentrum Jülich (FZJ), Germany. HHF tests were performed with a mean pulse duration

Table 1
Chemical composition of Fe(12–14)Cr–2W–0.3Ti–0.3Y_2O_3 ODS RAF steels (in wt.%).

Material	C	Si	Cr	W	Ti	Mn	Ni	Mo	Y	O	N
12Cr	0.045	0.141	11.8	2.05	0.25	0.12	0.038	0.006	0.25	0.46	0.033
14Cr	0.030	0.189	13.7	2.01	0.26	0.16	0.016	0.002	0.29	0.48	0.035

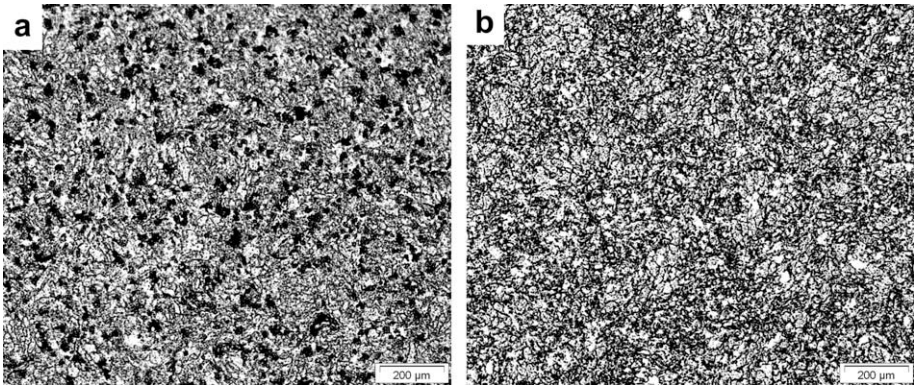

Fig. 1. Typical OM images of the (a) 12Cr and (b) 14Cr ODS RAF steels after HIPping.

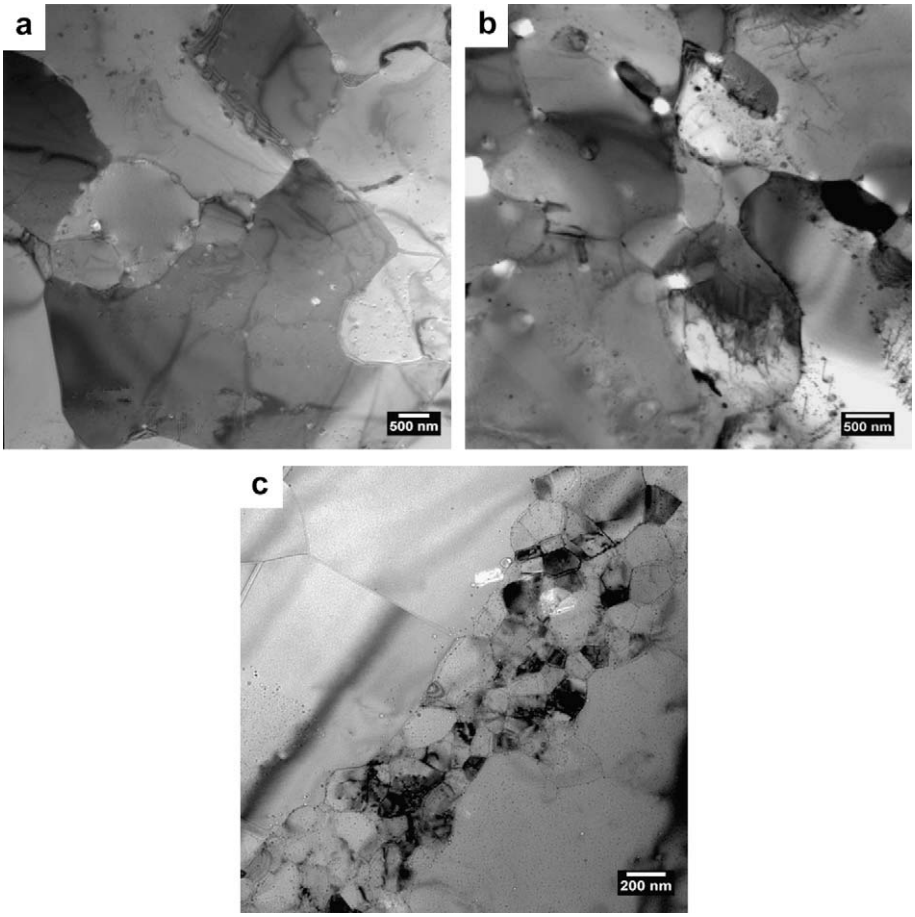

Fig. 2. Typical TEM images of the ODS RAF steels after HIPping (a) 12Cr, (b) 14Cr and (c) bimodal grain size.

of 5 ms and a power density in the range of 0.10 up to 0.40 GW/m^2. In the case of the 14Cr ODS steel single shots with different energy densities were applied. The same energy densities were applied onto the 12Cr material in one or 10 shots. Post-HHF testing characterisation was conducted by means of OM and profilometry.

3. Results and discussion

3.1. Microstructure examination of the specimens

Chemical compositions of the steels are reported in Table 1. Apart from the Cr and carbon contents the amounts of other elements are almost the same in both ODS RAF steel materials. 12Cr specimens exhibit slightly lower microhardness values (360 ± 17 $HV_{0.1}$) than 14Cr specimens (370 ± 13 $HV_{0.1}$), probably due to the lower chromium content and the slightly lower density exhibited by the former material (7.75 g/cm^3 for 12Cr specimens with respect to 7.78 g/cm^3 for 14Cr specimens). Note that the measured density values are more than 99.2% the theoretical density (7.82 g/cm^3).

OM and TEM images of the 12–14Cr ODS steels are shown in Figs. 1 and 2, respectively. In general, the microstructure of both consolidated materials is similar and consists of ferrite (α-Fe, bcc) with a bimodal distribution of coarse grains, a few micrometers in size (Fig. 2a and b), and smaller ones, about 100–500 nm in size (see Fig. 2c). The coarse grains are almost dislocation-free, while the smaller ones contain a higher number density of dislocations. This kind of bimodal microstructure results from the HIPping process and has been also observed by Kishimoto et al. [10], for instance. Oxide and carbide impurities (about a few hundred nanometers in size) and a high density of Y–Ti–O nano-clusters with an average size of about 5 nm are also observed in both kinds of steel (Fig. 3). Slightly larger nano-clusters are present in the 12Cr ingots (see Fig. 3a). Also, it should be emphasised that after HIPping residual porosity was seen in both materials. The pores were located preferentially at the grains boundaries of prior particles.

Tensile properties of the 12Cr and 14Cr ODS steel at room temperature and 750 °C are summarised in Table 2. Detailed description of tensile test is in Ref. [9].

In general, from the results presented in Table 2 it can be seen that there are no important differences in the mechanical properties of both ODS RAF steels. However, the 14Cr ODS material exhibits slightly higher ultimate tensile strength and yield strength but lower elongation values at room temperature and at 750 °C than the 12Cr alloy. It is well known that the higher the strength of material the easier the crack initiation and propagation after thermal shock experiment [11]. Since the tensile strength of the 14Cr ODS steel is higher and its elongation is lower than those of the 12Cr material, one may expect worse thermal properties for this alloy.

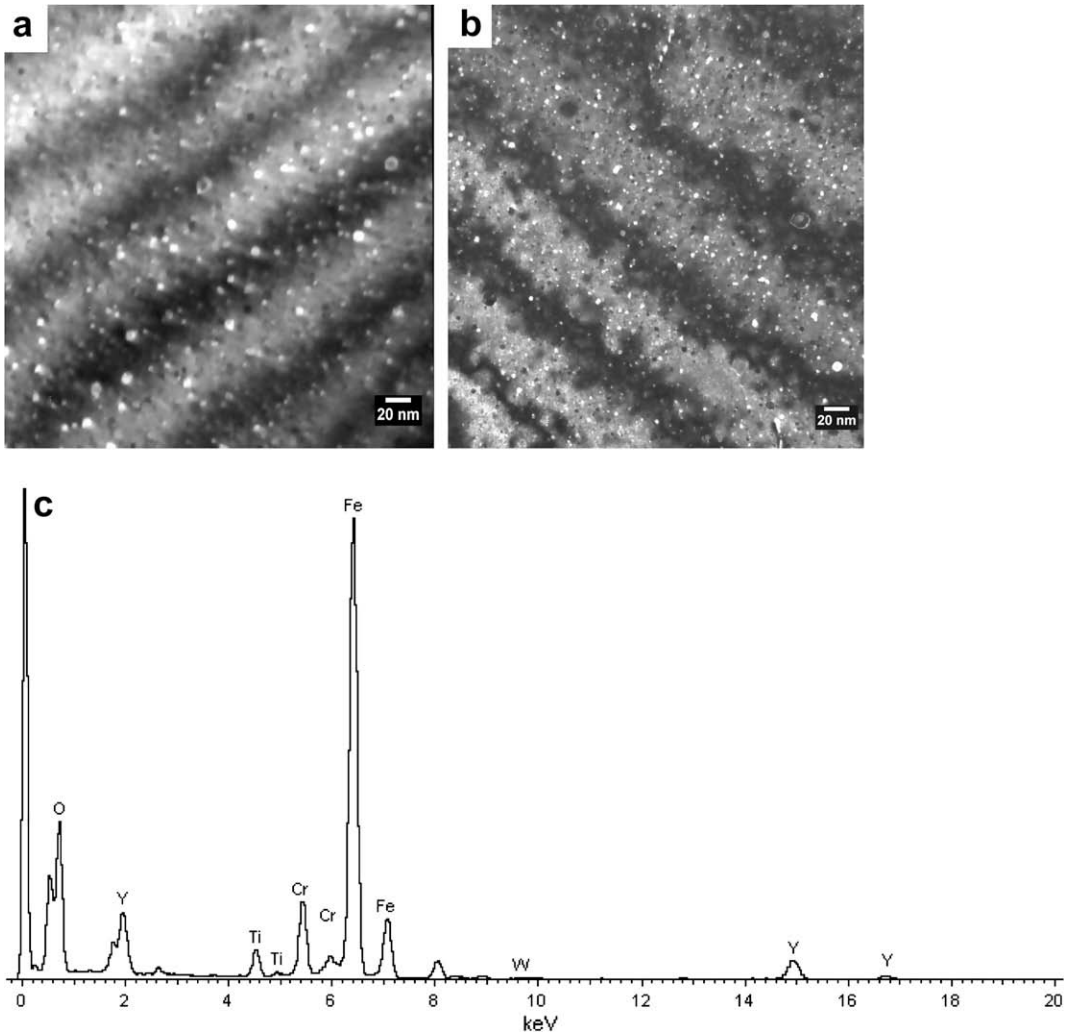

Fig. 3. TEM images of Y–Ti–O nano-clusters in the (a) 12Cr and (b) 14Cr ODS RAF steels and (c) EDS of the Y–Ti–O.

Table 2
Tensile tests results of the 12–14Cr ODS RAF steels at room temperature and 750 °C [after 9].

Material	Testing temperature (°C)	Tensile strength (UTS) (MPa)	Yield strength ($YS_{0.2}$) (MPa)	Total elongation (%)	Uniform elongation (%)	$YS_{0.2}$/UTS (%)
12Cr ODS RAF steel	23	930	780	16.8	10.1	84
	750	275	200	8.1	4.3	73
14Cr ODS RAF steel	23	955	830	12.2	6.2	88
	750	280	230	6.1	4.1	82

3.2. High heat flux testing of 12–14Cr ODS RAF steels

Various thermal energy densities from 0.75 up to 2.0 MJ/m^2 were applied onto the 14Cr material through single shots, accounting for a determined electron absorption coefficient of 0.68. The same energy densities were applied onto the 12Cr material in one or 10 repeated shots. For comparison of both ODS alloys, 10 shots were also applied onto the 14Cr material, with total energy density of 1 MJ/m^2. All thermal response data are presented in Table 3. This has been done since the thermal response after one (single) shot was found to be similar for both 12–14Cr ODS materials. This is also resulting from the similarity in the thermal conductivity (λ) values that have been calculated from the specific heat, the thermal diffusivity (presented in Table 4) and the density of the specimens.

Since the thermal conductivity has, besides the mechanical properties (yield and tensile strength), the strongest influence on the thermal shock behaviour and is responsible for the established thermal gradient in the materials, similar thermo-shock behaviours were found (compare images in Fig. 4). Therein the comparison of the ODS materials after applying 10 shots at 1.0 MJ/m^2 shows that the material response, not only from the temperature point of view but also from its microscopic appearance, is more or less identical for both materials. This fact, that the microstructure of both tested ODS materials after applying the same heat flux conditions is similar, offered the possibility to explore the materials in more detail. This comprises not only the onset of melting but also the evolution with repeated 10 shots (this is especially interesting for those loads where no effect had been found after the first shot).

The onset of melting occurs for an energy density between 1 and 1.5 MJ/m^2. For energy densities below the melting threshold only some kind of thermal etching of the material takes place (Fig. 5a), which highlights the material microstructure, i.e., the grain size and distribution. This material etching becomes more pronounced with increasing the number of shots. During melting the material exhibits enhanced bubble formation, leading to a peculiar surface structure in the centre of the loaded area, as shown in Fig. 5b. The analysis of the cross section (Fig. 6) revealed that this bubble formation results from the material recrystallisation and the formation of a columnar grain microstructure typical of molten re-solidified material. Thereby, the homogeneous melting depth increases with increasing power density from ~55 μm at 1.5 MJ/m^2 up to ~75 μm at 2.0 MJ/m^2. The same observation holds for the crater depth that forms due to material transport from the centre of the loaded area to its boundary and which amounts to ~90 μm at 1.5 MJ/m^2 up to ~190 μm at 2.0 MJ/m^2. The microstructure below the melting zone appears unaffected by the temperature

Table 3
Thermal response data of the 12–14Cr ODS RAF steels.

Specimens	Energy density (MJ/m^2)	Maximum temperature (°C)	Maximum temperature (°C)	Maximum temperature (°C)
		ε^* = 1	ε^* = 0.2	ε^* = 0.15
14Cr-1, 1 shot	0.75	583	1008	1103
14Cr-2, 1 shot	1.0	683	1157	1263
14Cr-2, 10 shots	1.0	708	1194	1304
14Cr-3, 1 shot	1.5	958	1568	1706
14Cr-4, 1 shot	2.0	1167	1880	2040
12Cr-1, 1 shot	0.75	667	1132	1237
12Cr-1, 10 shots	0.75	667	1132	1237
12Cr-2, 1 shot	1.0	708	1194	1304
12Cr-2, 10 shots	1.0	750	1257	1371
12Cr-3, 1 shot	1.5	958	1568	1706
12Cr-3, 10 shots	1.5	1083	1755	1906
12Cr-4, 1 shot	2.0	1167	1880	2040
12Cr-4, 10 shots	2.0	1208	1942	2107

ε^*: pyrometer data recorded with an IR-emissivity of "1" – recalculation of the emissivity according to the observed onset of melting of the loaded material (emissivity between 0.15 and 0.2 due to darkened observation window).

Table 4
Thermo-physical properties of the 12–14Cr ODS steels.

T (°C)	12Cr ODS			14Cr ODS		
	Thermal diffusivity (mm^2/s)	Specific heat (J/kgK)	Thermal conductivity (W/m K)	Thermal diffusivity (mm^2/s)	Specific heat (J/kgK)	Thermal conductivity (W/m K)
20	6.5	440.0	22.3	6.4	454.7	21.8
200	6.1	488.2	23.1	6.0	514.9	23.2
400	5.3	558.9	22.8	5.4	603.3	24.6
600	4.3	708.3	23.6	4.4	783.3	25.6
800	4.5	645.2	22.2	4.5	703.5	23.8

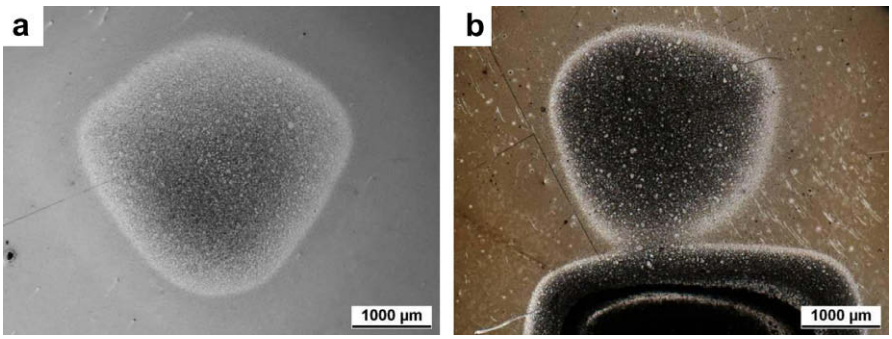

Fig. 4. OM images after HHF testing at $E = 1.0$ MJ/m^2 in 10 shots for the (a) 14Cr ODS and (b) 12Cr ODS RAF steels.

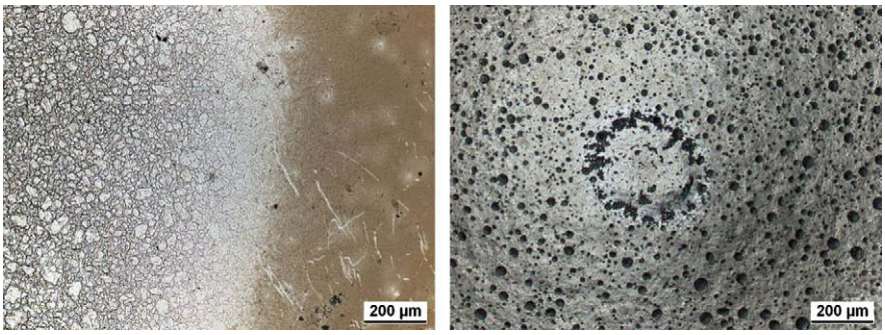

Fig. 5. OM images of the 12Cr ODS material after HHF testing at (a) $E = 1.0$ MJ/m^2 in 10 shots and (b) $E = 1.5$ MJ/m^2 in 10 shots.

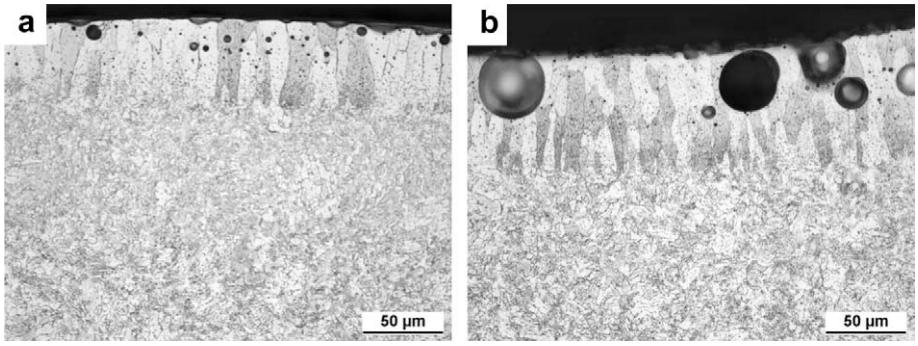

Fig. 6. OM images of the cross section of the 12Cr ODS material after HHF testing at (a) $E = 1.5$ MJ/m^2 in 10 shots and (b) $E = 2.0$ MJ/m^2 in 10 shots.

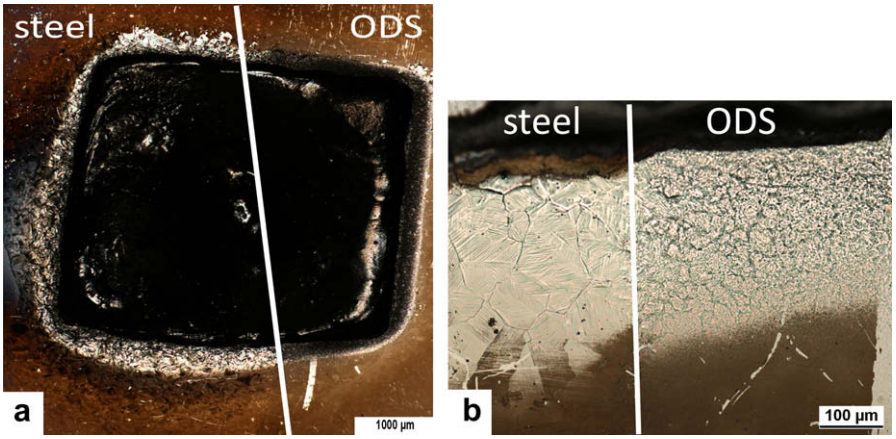

Fig. 7. OM images of the 12Cr ODS material after HHF testing at $E = 2.0$ MJ/m^2 in 10 shots; (a) overview; (b) high magnification of the lower boundary area. *Steel refers to 316L stainless steel, **ODS refers to 12Cr ODS ferritic steel.

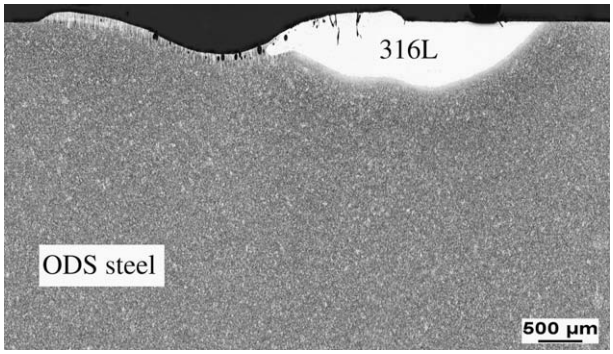

Fig. 8. OM images of a cross section of the 12Cr ODS material after HHF testing at $E = 2.0$ MJ/m^2 in 10 shots.

exposure during the thermal shock. It seems that in the case of both ODS materials the yield strength is high enough to avoid plastic deformation of the specimens before reaching the melting point.

Some remaining part of the stainless steel can (grade 316L) used for the HIPping process, in which the powder was degassed and closed, was found on the top surface of a specimen of the 12Cr ODS steel. Thus, a comparison of the thermal resistance of the 316L stainless steel and the developed ODS material to HHF at 2.0 MJ/m^2 was possible. In Fig. 7a it is shown that half of the loaded spot was situated in the stainless steel (left) and half of it in the ODS material (right). Significant differences can be seen between both areas, which become more apparent at higher magnification (Fig. 7b). The thermally etched part refers to the ODS steel, while the adjacent plastically deformed area refers to the stainless steel. The affected areas, in terms of length and depth are equivalent for both materials (Fig. 8), indicating an identical thermal conductivity. The differences resulting in plastic deformation and heavy crack formation in the stainless steel (Fig. 8, in which the white area represents the stainless steel part) are therefore only related to the mechanical material properties which are, as expected, superior for the ODS material.

4. Conclusions

Two ODS RAF steel grades with 12 and 14 wt.% Cr were fabricated by mechanical alloying and HIPping and exposed to single and multiple (10×) transient thermal loads between 0.75 and 2.0 MJ/m^2 for 5 ms, typical of nuclear fusion devices. Besides slight differences in the mechanical properties, which may suggest that the material with lower yield strength (higher elongation) may have better thermal properties, both ODS materials show similar thermal conductivity and thermal shock behaviour with a melting threshold between 1.0 and 1.5 MJ/m^2. Below this threshold the materials exhibit a modification of the exposed surface similar to thermal etching, which becomes more pronounced under multiple loads. No crack damage was observed at the surface of the ODS steel specimens. Thermal loads above the melting threshold lead to material movement from the centre to the boundary of the loaded area and therefore to the formation of a crater. Furthermore, bubble formation occurs related to columnar recrystallization in the molten and re-solidified material. In contrast to 316L stainless steel the two ODS grades show neither plastic deformation nor crack formation, in relation to their higher mechanical strength.

Finally, it is important to emphasise that there are no significant differences in the microstructure and thermal shock response between 12Cr and 14Cr ODS ferritic steels and both ODS alloys do not form cracks under the applied loads which is, compared to other potential plasma facing materials, with respect to first wall applications especially tungsten or tungsten coatings, a significant improvement. Furthermore, for regions with first wall temperatures above the melting temperature of the ODS steels, they may also act as substrate for tungsten coatings, knowing that in case of the accidental loss of the coating the material can withstand the applied power loads for a certain time.

Acknowledgements

The Paul Scherrer Institute is acknowledged for the overall use of the facilities. This work, supported by the European Communities under the contract of Association between EURATOM/Confédération Suisse, was carried out within the framework of the European Fusion Development Agreement. The views and opinions expressed herein do not necessarily reflect those of the European Commission. This work was also performed within the framework of the Integrated European Project "ExtreMat" (contract NMP-CT-2004-500253) with financial support by the European Community. It only reflects the view of the authors and the European Community is not liable for any use of the information contained therein.

References

[1] S. Ukai, A. Mizura, T. Yoshitake, T. Okuda, M. Fujiwara, S. Hagi, T. Kobayashi, J. Nucl. Mater. 283–287 (2000) 702–706.
[2] M.K. Miller, D.T. Hoelzer, E.A. Kenik, K.F. Russell, J. Nucl. Mater. 329–333 (2004) 338–341.
[3] D. Sakuma, S. Yamashita, K. Oka, S. Ohnuki, E. Wakai, J. Nucl. Mater. 329–333 (2004) 392–396.
[4] T. Hirai, H. Maier, M. Rubel, Ph. Mertens, R. Neu, E. Gauthier, J. Likonen, C. Lungu, G. Maddaluno, G.F. Matthews, R. Mitteau, O. Neubauer, G. Piazza, V. Philipps, B. Riccardi, C. Ruset, I. Uytdenhouwen, Fusion Eng. Des. 82 (2007) 1839–1845.
[5] D. Maisonnier, I. Cook, P. Sardain, L. Boccaccini, L. Di Pace, L. Giancarli, P. Norajitra, A. Pizzuto, P.P.C.S. Team, Design 75–79 (2005) 1173–1179.
[6] R. Lässer, N. Baluc, J.-L. Boutard, E. Diegele, S. Dudarev, M. Gasparotto, A. Möslang, R. Pippan, B. Riccardi, B. van Der Schaaf, Fusion Eng. Des. 82 (2007) 511–520.
[7] P. Norajitra, L.V. Boccaccini, E. Diegele, V. Filatov, A. Gervash, R. Giniyatulin, S. Gordeev, V. Heinzel, G. Janeschitz, J. Konys, W. Krauss, R. Kruessmann, S. Malang, I. Mazul, A. Moeslang, C. Petersen, G. Reimann, M. Rieth, G. Rizzi, M. Rumyantsev, R. Ruprecht, V. Slobodtchouk, J. Nucl. Mater. 329–333 (2004) 1594–1598.
[8] Z. Oksiuta, N. Baluc, J. Nucl. Mater. 374 (2008) 178–184.
[9] Z. Oksiuta, N. Baluc, in: Proc. 22nd IAEA Fusion Energy Conference (FEC), 13–18 October, 2008, Geneva.
[10] H. Kishimoto, M.J. Alinger, G.R. Odette, T. Yamamoto, J. Nucl. Mater. 329–333 (2004) 369–371.
[11] T. Hatano, S. Suzuki, K. Yokoyama, T. Kuroda, M. Enoeda, J. Nucl. Mater. 283–287 (2000) 685–688.